Comparison of structural and spectroscopic properties of Ho3+-doped niobate compounds

Simon Guené-Girard, Julia Courtois, Marc Dussauze, Jean-Marc Heintz, Alexandre Fargues, Jérôme Roger, Marcelo Nalin, Thierry Cardinal, Veronique Jubera

Comparison of structural and spectroscopic properties of Ho^{3+}-doped niobate compounds

S. Guene-Girard[1], J. Courtois[1], M. Dussauze[2], J-M. Heintz[1], A. Fargues[1], J. Roger[3], M. Nalin[4], T. Cardinal[1], V. Jubera[1]*

1 - CNRS, Univ. Bordeaux, Bordeaux INP, ICMCB, UMR 5026, F-33600 Pessac, France

2 – ISM- Institute of Molecular Science, UMR 5255 CNRS-University of Bordeaux, 33405 Talence, France

3- Université de Bordeaux, CNRS, Laboratoire des Composites ThermoStructuraux, UMR 5801, 33600 Pessac, France

4- Chemistry Institute, São Paulo State University – UNESP, 14800-060, Araraquara, SP, Brazil

* corresponding author: Pr. V. Jubera, ICMCB-CNRS, 87 avenue du Dr Albert Schweitzer, 33608 Pessac Cedex, France; veronique.jubera@u-bordeaux.fr

Key words: rare earth, niobate, luminescence, Raman, energy transfer

Abstract Ho^{3+}-doped $YNbO_4$ and Y_3NbO_7 phosphors were synthesised via a co-precipitation synthesis route. Structural characterisation and spectroscopic properties were performed as a function of the Ho^{3+} concentration. The Rietveld type-refinement confirms the stabilisation of the pure monoclinic Fergusonite $YNbO_4$ phase at the highest temperatures, but the quadratic phase is stabilised for the lowest temperature, whereas a pure cubic fluorite Y_3NbO_7 phase was observed for all of the heat treatments. Raman and infrared spectroscopies were used to compare the cation-oxygen vibrational modes. Emission spectra and up-conversion processes were obtained under excitation at 445 and 975 nm respectively. For a similar Ho^{3+} content, the energy transfers observed show differences between the two crystalline compounds that are related to a stronger interaction between the holmium cations in the fluorite host lattice.

1- Introduction

The ongoing development of 1.7-2.7 µm highly energetic compact sources can contribute to the improvement in the efficiency of optoelectronic devices for many applications and will be beneficial to society. The 1.7-2.7 µm optical window covers the eye-safe spectral region, enabling its use in medical applications. In addition, such laser sources can be optimised for optical communication and the defence applications. They can also act as efficient pumping

sources for transition-metal-doped semiconductors, chalcogenide glasses, and optical parametric oscillators [1-3]. Currently, only a few crystalline active emitting materials are available such as rare-earth-doped sesquioxides [4], YAG and LuAG garnets [5], CaF_2 [6], KGW, and (K,Na)NbO_3 [7]. Therefore, the proposed alternative compositions with different local environments in terms of coordination number or symmetry of the doping element should broaden the existing absorption and emission wavelength ranges.

The choice of Ho^{3+} as the doping element is based on its rich energy diagram. Ho^{3+} can enable the generation of radiative emissions in the visible, near, and mid-infrared regions [8-10]. It is easily excited with a commercial diode in the visible and near-infrared range or by a crystal-based laser source such as a Tm-doped YLF laser source that is suitable for the direct excitation of the $^5I_7$ level of Ho^{3+} that produces the 2 µm laser radiation. Owing to the significant number of energy levels, a high dopant concentration within the host lattice give rise to energy transfer between the Ho^{3+} ions. These phenomena can be studied by tracking the intensity ratio of the 4f-4f lines along the UV-mid infrared spectral window as well as the up-conversion processes under near-infrared excitation [10]. Then, the composition must be optimised to favour the emission from a specific level suitable for the targeted application.

In this study, Ho^{3+}-doped compounds in the Y_2O_3-Nb_2O_5 phase diagram were considered for their transmission up to 4 µm in the IR (as $LiNbO_3$ single crystal [11]). Both Ho^{3+}-doped $YNbO_4$ and Y_3NbO_7 particles were synthesised via the co-precipitation synthesis route. The structural and spectroscopic properties of the particles were characterized and compared as a function of the doping element concentration.

2- Materials and methods

2.1 Particle syntheses

Both Ho^{3+}-doped $YNbO_4$ and Y_3NbO_7 particles were prepared by a co-precipitation process. $NbCl_5$ (99.9% purity, Aldrich), $HoCl_3.6H_2O$ (99.99% purity, Merck), and $YCl_3.6H_2O$ (99.99% purity, Alfa Aesar) were used for the synthesis. The concentration of Ho^{3+} was varied between 0.25% and 10% (molar substitution of yttrium cations) depending on the niobate compound. The chloride rare-earth compounds were dissolved in distilled water, whereas the chloride niobate was dissolved in HCl acid and then poured with the rare earth solution in stoichiometric proportions. Aqueous ammonia was chosen to precipitate the solid particles and was slowly introduced under stirring into the acid cationic solution. The pH was maintained at nine during the entire procedure. The suspensions were aged for 3 days and then cleaned and centrifuged with distilled water in the first step and absolute ethanol in a second step. This procedure was

repeated several times. The finally obtained particles were dried and heat-treated at the temperatures ranging from 700 to 1300 °C for Ho^{3+}-$YNbO_4$ ($Y_{1-x}Ho_xNbO_4$) and from 700 to 1100 °C for Ho^{3+}-Y_3NbO_7 ($Y_{3(1-x)}Ho_{3x}NbO_7$).

2.2 Chemical analysis

Chemical analysis of the particles was performed using inductively coupled plasma-optical emission spectrometry (ICP/OES) carried out using a Varian ICP/OES 720 ES apparatus. H_2SO_4 was used to dissolve the Ho^{3+}-Y_3NbO_7 compounds, whereas the use of a HNO_3/HCL and HNO_3/HF acid mixture coupled with microwave heat treatment was necessary to fully mineralise holmium/yttrium and niobium from Ho^{3+}-$YNbO_4$.

Thermodynamics

Thermodynamic calculations were performed for the Nb_2O_5-Y_2O_3 system using the Thermo-Calc software [12]. The relevant TCOX8 database was used for these calculations [13].

2.3 X-Ray diffraction (XRD)

Powder X-ray diffraction patterns were obtained using a Philips X'Pert MPD X-ray diffractometer in Bragg-Brentano geometry using Cu K_α1,2 radiation in the 2θ range of 8–75°, with a step of 0.02° and a counting time of 30 s. The unit cell parameters, zero-shift, atomic positions, and peak profile parameters were refined for all diffractograms using the FullProf software package.

Scanning electronic microscopy (SEM)

Scanning electron microscopy (SEM) analysis was performed using a JEOL field-emission gun scanning electronic microscope (FEG-SEM) to characterise the morphology of the powder.

2.4 Raman and infrared spectroscopies

Unpolarized Raman spectra were obtained with a Horiba Xplora spectrometer using a 785 nm excitation line with an incident power of 10 mW. Raman spectra were recorded using a 100x objective, in the range of 200–1200 cm^{-1} with a resolution of 2.5 cm^{-1}.

Diffuse reflectance infrared Fourier transform (DRIFT) measurements were carried out using a Praying Mantis diffuse reflection accessory (Harrick Scientific) housed in an FTIR spectrometer (Nicolet 6700). The sample was blended with dried KBr (1% in ratio) and placed in an adjustable microsampling cup (volume of 0.3 mL, diameter of 3 mm) using a funnel. In DRIFT, accessory spherical mirrors form a highly efficient diffuse reflection illumination and collection system. The specific configuration of the Praying Mantis minimises the detection of specular components. The experimental and background spectra were acquired using the Omnic software.

2.5 Luminescence spectroscopy

The excitation and emission spectra were obtained using a Horiba Jobin Yvon Fluorolog 3 equipped with a xenon lamp (450 W). A 455 nm laser diode source was used to perform the infrared luminescence measurements. A photomultiplier tube (PMT, Hamamatsu R298, Japan) and InGaAs and PbSe detectors were used for visible, near-, and mid-infrared detection, respectively. All of the measurements were performed at room temperature. Luminescence spectra were corrected for the variation of the lamp, equipment geometry, and sensitivity of the detectors. The correction curve was constructed using a calibrated W lamp.

The decay times were measured using time-resolved spectroscopy. A Continuum Surelite SL II - 10 laser (355 nm, 10 Hz, 70 mJ, 4-6 ns) was used to excite an OPO (Panther Ex, Electro-optics, Inc.) in order to obtain a 455 nm pulsed excitation wavelength. A monochromator and a gated ICCD camera (Andor) recorded the emission spectra that were optically synchronised using a pulsed laser.

3- Results and discussion

3.1 Chemical analysis of the powder.

The composition of the materials was examined using ICP to confirm that the desired holmium concentration within the host lattice was achieved. Table 1 lists the target and final compositions of the synthesised powders.

Table 1- Chemical compositions of the Ho^{3+}-doped niobate compounds.

$YNbO_4$				
Targeted [Ho^{3+}] mol concentration in cation % (number of ions/cm^3)	Targeted [Ho^{3+}] mass %	ICP determination of [Ho^{3+}] mass % +/-0.01%	Experimental corresponding cation mol %	Sample label
0.25 ($0.34x10^{20}$)	0.17	0.17	0.25	YNHo025
0.5 ($0.68x10^{20}$)	0.33	0.30	0.45	YNHo05
1 ($1.36x10^{20}$)	0.67	0.62	0.93	YNHo1
2 ($2.73x10^{20}$)	1.33	1.39	2.08	YNHo2
3 ($4.09x10^{20}$)	1.99	1.96	2.95	YNHo3
Y_3NbO_7				
1 ($2.1x10^{20}$)	1.04	0.4	0.39	Y3NHo04
2 ($4.1x10^{20}$)	2.08	0.63	0.6	Y3NHo06
5 ($10x10^{20}$)	5.12	1.93	1.86	Y3NHo2
8 ($17x10^{20}$)	8.08	2.88	3.06	Y3NHo3
10 ($21x10^{20}$)	10.01	3.62	3.83	Y3NHo4

ICP titration revealed that the final composition was strongly dependent on the stoichiometry of the matrix. The values obtained for Ho^{3+}-$YNbO_4$ were in good agreement with the targeted

compositions, whereas a significant discrepancy was observed for the Ho^{3+}-Y_3NbO_7 compounds. The latter belong to a solid solution domain in the Y_2O_3-Nb_2O_5 phase diagram (Figure 1) that is found between the Nb contents of approximately 21 % and 28 % (molar ratio) [14,15]. The yttrium and niobium concentrations were measured to determine the final cationic ratio. Considering the experimental error of the measurements, the final cationic ratios are close to 23% (Table SI1), indicating the presence of a competitive kinetic process during the co-precipitation synthesis route between yttrium and the other cations for the Ho^{3+}-Y_3NbO_7 compound. The final sample labels have been chosen in agreement with the experimental ICP measurements and not as function of the targeted Ho^{3+} compositions.

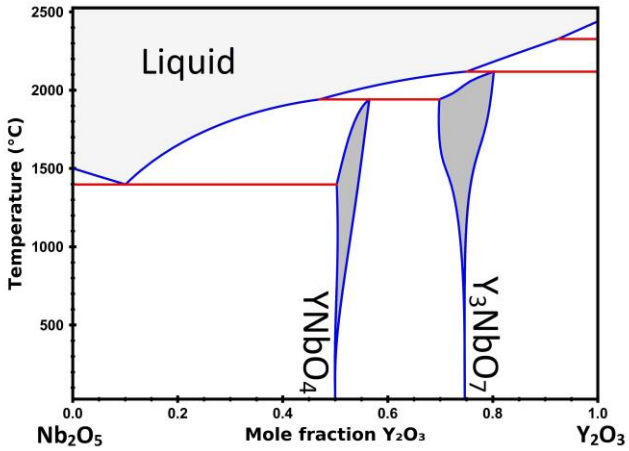

Figure 1- Calculated phase diagram of Nb_2O_5-Y_2O_3 [13].

3.2 Thermodynamic calculations

The Gibbs free energies of the formation of $YNbO_4$ and Y_3NbO_7 from Y_2O_3 and Nb_2O_5 were calculated in the temperature range of 500–1500 °C. The corresponding curves are shown in Figure 2. For easier comparison, the Gibbs energies were reported for one mole of the component in each phase. Negative values were obtained for all compositions, confirming the favourable formation of each phase. The values for $YNbO_4$ (in fact $Y_{\frac{1}{6}}Nb_{\frac{1}{6}}O_{\frac{4}{6}}$) are more negative than those for Y_3NbO_7 (in fact, $Y_{\frac{3}{11}}Nb_{\frac{1}{11}}O_{\frac{7}{11}}$). Thus, $YNbO_4$ is more stable than Y_3NbO_7. This higher stability can explain the finding that $YNbO_4$ is more easily stabilised and doped with Ho^{3+} cations. Consequently, the content of Ho^{3+} in this phase is expected to be in accordance with the content introduced in the raw material batch. Moreover, regarding the final temperatures of heat treatment, the homogeneity range of $YNbO_4$ at 1300 °C was found to be larger than that of Y_3NbO_7 at 1100 °C, as shown in Figure 1. $YNbO_4$ remained stable despite a larger deviation from the stoichiometry. It is highly likely that this difference also promotes the stability of Ho^{3+} doping.

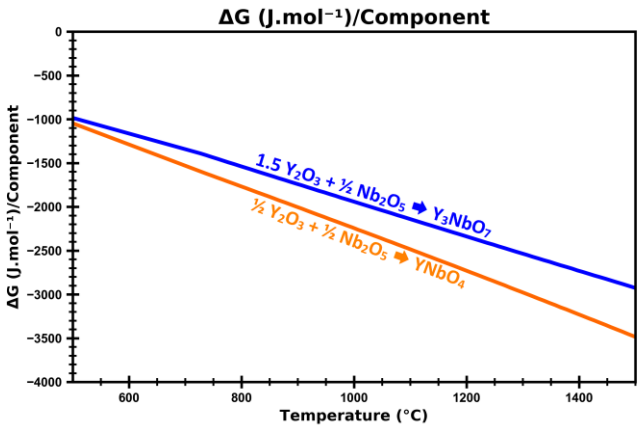

Figure 2- Curves of the Gibbs free energies of formation of $YNbO_4$ and Y_3NbO_7 between 500 and 1500 °C for 1 mole of the chemical components i.e. $Y_{\frac{1}{6}}Nb_{\frac{1}{6}}O_{\frac{4}{6}}$ and $Y_{\frac{3}{11}}Nb_{\frac{1}{11}}O_{\frac{7}{11}}$ [13].

3.3 Structural and morphological characterization of the Ho^{3+} doped niobate compounds

The diffractograms of the Ho^{3+}-doped powders are presented in Figure 3. An intermediary heat treatment was applied to the coprecipitated powders, and X-ray diffraction patterns were obtained to follow the evolution of the crystallisation. Surprisingly, the temperature evolution shows the coexistence of the tetragonal and monoclinic phases at the lowest temperatures, while a pure monoclinic phase was observed at 1300 °C (Figure 3a). Indeed, $YNbO_4$ presents two allotropic varieties. As described in refs. [16,17], the low-temperature unit cell possesses monoclinic symmetry crystallising in the *C*2/*c* space group. A phase transition is expected at approximately 858 °C to stabilise the tetragonal unit cell (space group $I4_1/a$). The co-existence of two varieties of the same compound synthesised at the nanoscale has also been reported for different oxides such as ZrO_2 [18-21] and HfO_2 [22]. This can be attributed to the high surface energy of the nanoparticles and some disparity in the size of the $YNbO_4$ grains. The grain growth induced by the heat treatments enables the gradual disappearance of the low-temperature metastable tetragonal phase in favour of the monoclinic phase when the critical size of the crystallites is reached. The concentration of rare earth as a doping element can also play a role in this process, as described for HfO_2[22]. However, the dwell time duration and the cooling process applied during the synthesis (natural cooling applied after the dwell time) appear to quench the system into the monoclinic phase, so that the diffraction peaks of the tetragonal phase are not observed even at the highest temperature of treatment. Such stabilisation of the Fergusonite monoclinic phase above the transition temperature was also observed for the nanocrystals prepared under hydrothermal conditions and post heat treatment at 1300 °C. Using this experimental procedure, the XRD fingerprint of the tetragonal phase was

detected in addition to that of the monoclinic phase [23]. For our material, the corresponding cell parameters obtained after the Lebail refinement of the monoclinic Fergusonite phase crystallising in the *C2/c* space group are *a*= 7.623(1) Å, *b*= 10.952(1) Å *c*= 5.301(2) Å *β*=138.44(1), and no trace of the quadratic variation was detected [24,25]. The presence of Ho^{3+} does not change the diffractograms; however, for the highest concentration, additional small peaks in the 20°-30° region can be attributed to traces of Nb_2O_5 (Figure SI1). A pure cubic fluorite Y_3NbO_7 phase *a*= 5.241(1) Å, space group Fm-3m [26,27] was also obtained regardless of the temperature, with satisfactory reliability factors for the highest heat treatment (Bragg R-factor : 0.21, Rf-factor : 0.27) (Figures 3c,d). An increasing of the crystallite sizes from 15 nm at 700 °C to 30 nm is reflected by thinner diffraction peaks observed for the highest temperature (calculations performed according to the Debye-Sherrer law). Because of the close values of the yttrium and holmium cationic radii (rY^{3+}=0.90 Å; rHo^{3+}=0.901 Å for (CN=6)), no significant change in the cell parameters as well as in the diffraction peaks shape was observed as a function of Ho^{3+} doping rate (Figure SI1).

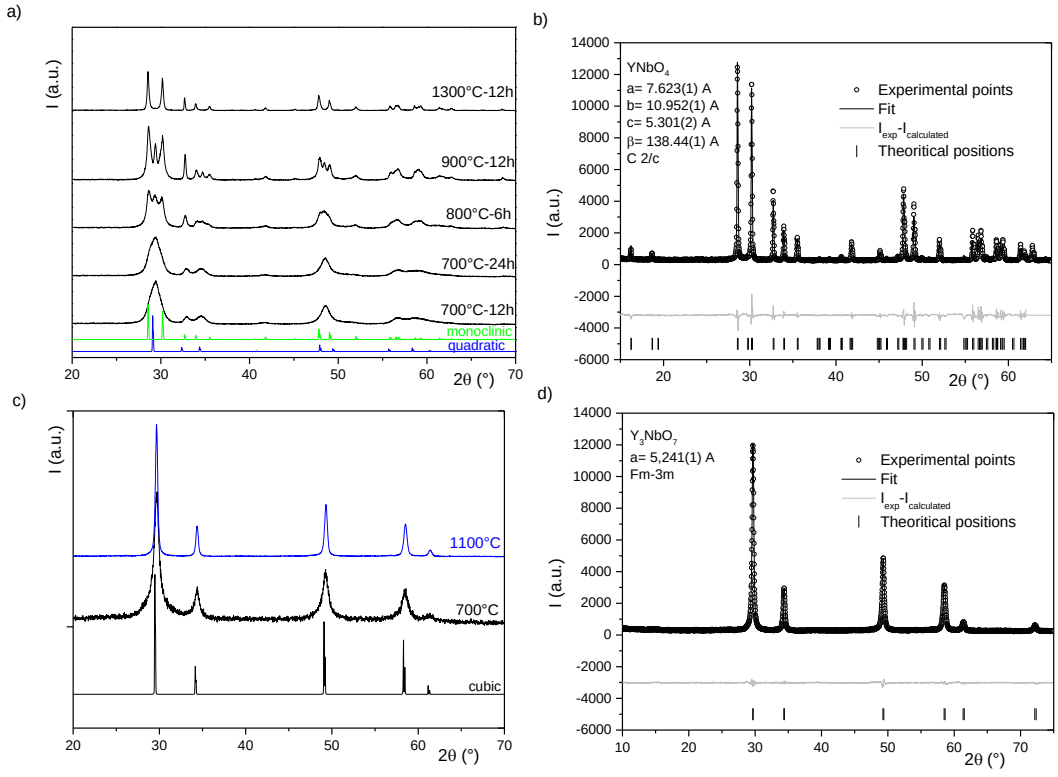

Figure 3- Diffractograms and Rietveld type-refinement of the Ho^{3+}-doped niobate: Ho^{3+} $YNbO_4$ (a,b); Ho^{3+} Y_3NbO_7 (c,d). (i), (ii) and (iii) are theoretical diffraction peaks calculated from the cif files $YNbO_4$ monoclinique: Collection Code 239207, $YNbO_4$ tetragonal: Collection Code 239209, Y_3NbO_7: Collection Code 109064 (JCPDS file number $YNbO_4$-monoclinique: 00-023-1486, $YNbO_4$ tetragonal: 00-038-0187; Y_3NbO_7: 01-074-6421 respectively).

The shape and intensity of the diffraction peaks indicate good crystallinity of the $YNbO_4$ and Y_3NbO_7 powders for the heat treatment at 1300 °C and 1100 °C, respectively. Thus, all optical characterisations were performed on Ho^{3+} powders heat-treated at these temperatures.

SEM images were obtained to visualise grain constitution and morphology. The results for the composition with the lowest doping are presented in Figure 4 for the samples obtained with heat treatments at different temperatures.

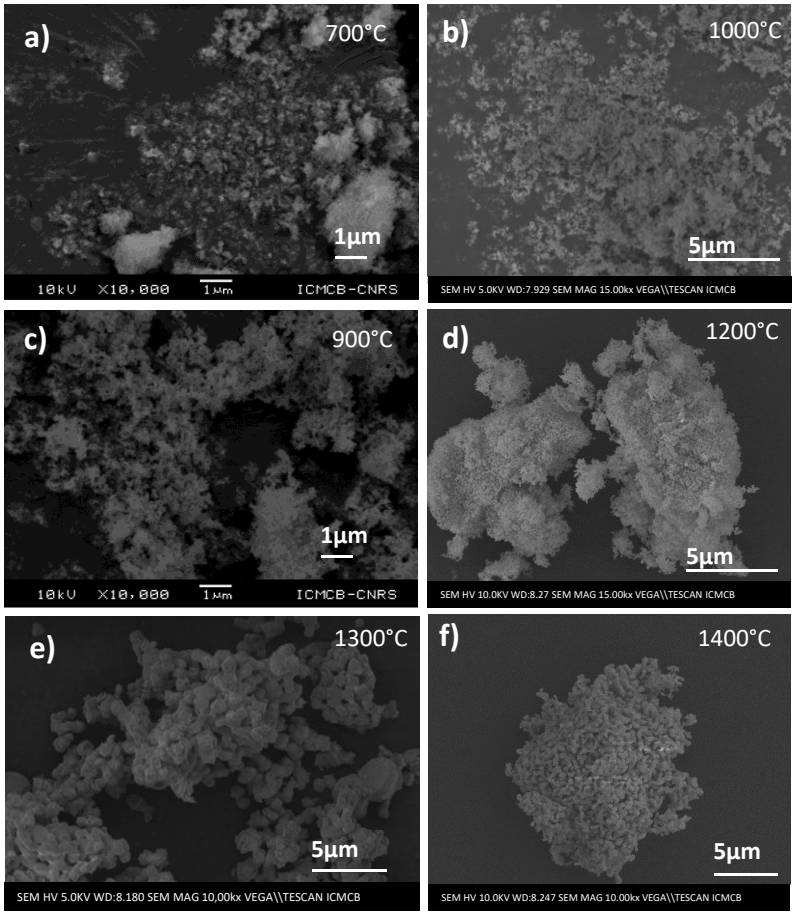

Figure 4-SEM images of the Ho^{3+}-doped niobate compounds: 0.25%-Ho^{3+} $YNbO_4$ (a,c,e; targeted composition); 1% Ho^{3+} Y_3NbO_7 (b,d,f; targeted composition) obtained with heat treatments at different temperatures.

For the lowest heat-treatment temperature, the powder was composed of nanometric small grains of both compositions. The low temperature favours the aggregation of compounds in large micrometric porous grains. For the highest temperature, at the same magnification, the sintering process appears to be more advanced for the monoclinic Fergusonite compound.

Indeed, the Ho^{3+}-$YNbO_4$ powders were composed of large micrometric grains (10-15 µm) (Figure 4e). Within the grains, micrometric crystallites are aggregated, showing that the heat treatment applied after the synthesis route (1300 °C) is high enough to favour their growth and sintering.

The smaller size of the Ho^{3+}-Y_3NbO_7 grain (approximately 100 nm at 1000 °C) is confirmed by microscopy and is in agreement with the observed diffraction peak shapes discussed above (Figures 3c, 4b; higher magnifications are not shown here): the size of crystallites obtained by Rietveld refinements is approximately 25 nm, regardless of the Ho concentration, implying that the nanometric grains are comprised by a few crystallites. The compaction rate of these agglomerates appears to be lower (cloudy aspect), indicating that the heat treatment applied at 1000 °C is not sufficient to aggregate the crystallites. Heat treatments at 1200 °C and 1400 °C resulted in the formation of large micrometric porous aggregates, but the size of the grain remains much smaller than that observed for the Fergusonite compound.

3.4 Characterization by vibrational and luminescence spectroscopies

Raman and infrared spectroscopies enable the identification and comparison of cation-oxygen vibrational modes. Owing to the high molar weight of the rare earth element, under the applied experimental conditions, these spectroscopic techniques are suitable for the analysis of niobate environments. The 785 nm excitation wavelength was preferred to limit the contribution of Ho^{3+} luminescence to the global response. The obtained Raman spectra are shown in Figure 5.

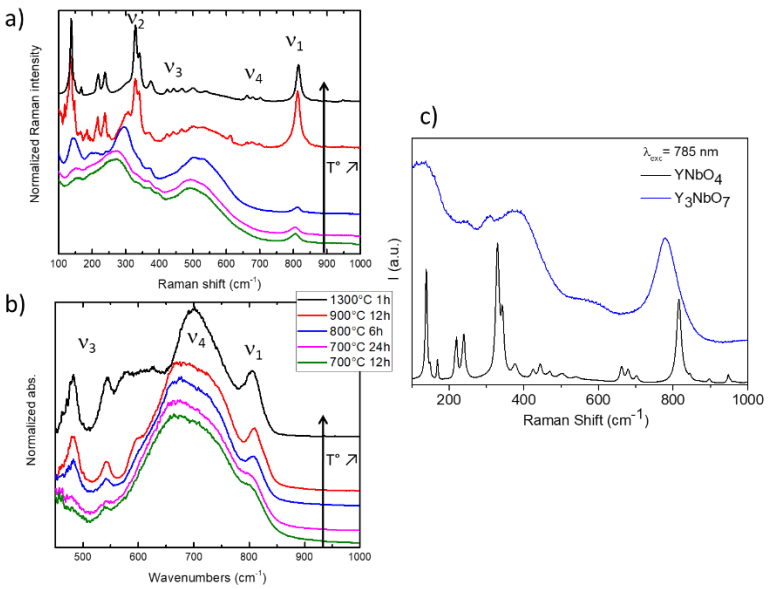

Figure 5- Raman spectroscopy of the niobate particles: Raman (a) and infrared (DRIFT) (b) spectra of the $YNbO_4$ compounds synthesized with various heat-treatment temperatures, Raman spectra of $YNbO_4$ and Y_3NbO_7 heat treated at 1300 and 1100 °C, respectively (c).

Based on the X-ray diffraction study of $YNbO_4$, we expect that a phase transition from a quadratic to a monoclinic crystalline structure will be obtained by increasing the heat treatment temperature. The compound heat treated at 700 °C showed broad bands for both IR and Raman responses with two main Raman maxima at 500 and 275 cm^{-1} and a maximum at 690 cm^{-1} in the IR spectrum and a small contribution at 800 cm^{-1} for both spectra. Increasing the heat treatment temperature to 800 °C induced a slight narrowing of the bands in the low-frequency Raman range with two clear contributions peaking at 310 and 150 cm^{-1}. For powders treated above 800 °C, new Raman bands can be observed at 350 and 370 cm^{-1} together with a clear increase in the high-frequency band at 800 cm^{-1}. Similarly, in the IR spectrum, the intensity of the band at 800 °C increased, the main contribution was narrower and shifted to 720 cm^{-1}, and two other bands at 480 and 520 cm^{-1} clearly increased with the heat treatment temperature above 800 °C.

The Raman spectra measured for the $YNbO_4$ heat-treated at 900 and 1300 °C are in agreement with those reported by Blasse [28] for the monoclinic phase. The spectral assignment proposed by these authors is based on a tetrahedral environment of the niobium for which the Raman (υ_1 and υ_2) and IR (υ_3 and υ_4) active modes, expected for a Td local symmetry of the niobium cations, were proposed. As noted above and depicted in Figure 5, both the Raman and IR spectra obtained for the quadratic phase are quite different, indicating a significant change in the niobium coordination. This is consistent with the description of the quadratic phase on the basis of X-ray diffraction data given originally by Kinzhibalo et al. [29] and recently confirmed by Arulnesan et al. [30] that describes the environment of niobium in the quadratic phase as a highly distorted six-coordinate geometry with two long (~2.5 Å) and four short (~1.9 Å) Nb–O distances.

Figure 5c compares the Raman spectra of fluorite Y_3NbO_7 and monoclinic $YNbO_4$. In the first approach, we focus on the difference in the niobium cation local symmetry (octahedral for Y_3NbO_7 and tetrahedral for $YNbO_4$) to explain the frequency shifts observed for all of the Raman bands. It is observed that the Raman peaks are clearly better defined for the monoclinic $YNbO_4$ than for the Y_3NbO_7 matrix. A significant broadening of the peaks was observed for the fluorite Y_3NbO_7 compound. This indicates the presence of local disorder due to the statistical distribution of oxygen vacancy locations: 1 anionic position out of 8 must be empty to maintain the charge neutrality of the host lattice. It should also be noted that such a characteristic of disorder is not observed in the XRD patterns. Such a discrepancy between the Raman spectra and X-ray diffraction patterns has already been observed for the niobium

compounds, for example in the highly crystalline $Bi_{0.5}Nb_{0.5}Te_3O_8$ systems [31]. The authors suggest the existence of an anionic disorder in the short and medium ranges. For Y_3NbO_7, Kovyazina et al.[32] also proposed the existence of a local ordering of the oxygen vacancies resulting in the stabilization of the pyrochlore domains. However, even if they exist, these pyrochlore domains are too small to be detected by X-ray diffraction.

Luminescence spectroscopy was performed for the samples with different Ho^{3+} concentrations. Figure 6 illustrates the emission intensity variation from 480 to 2200 nm obtained in these experiments.

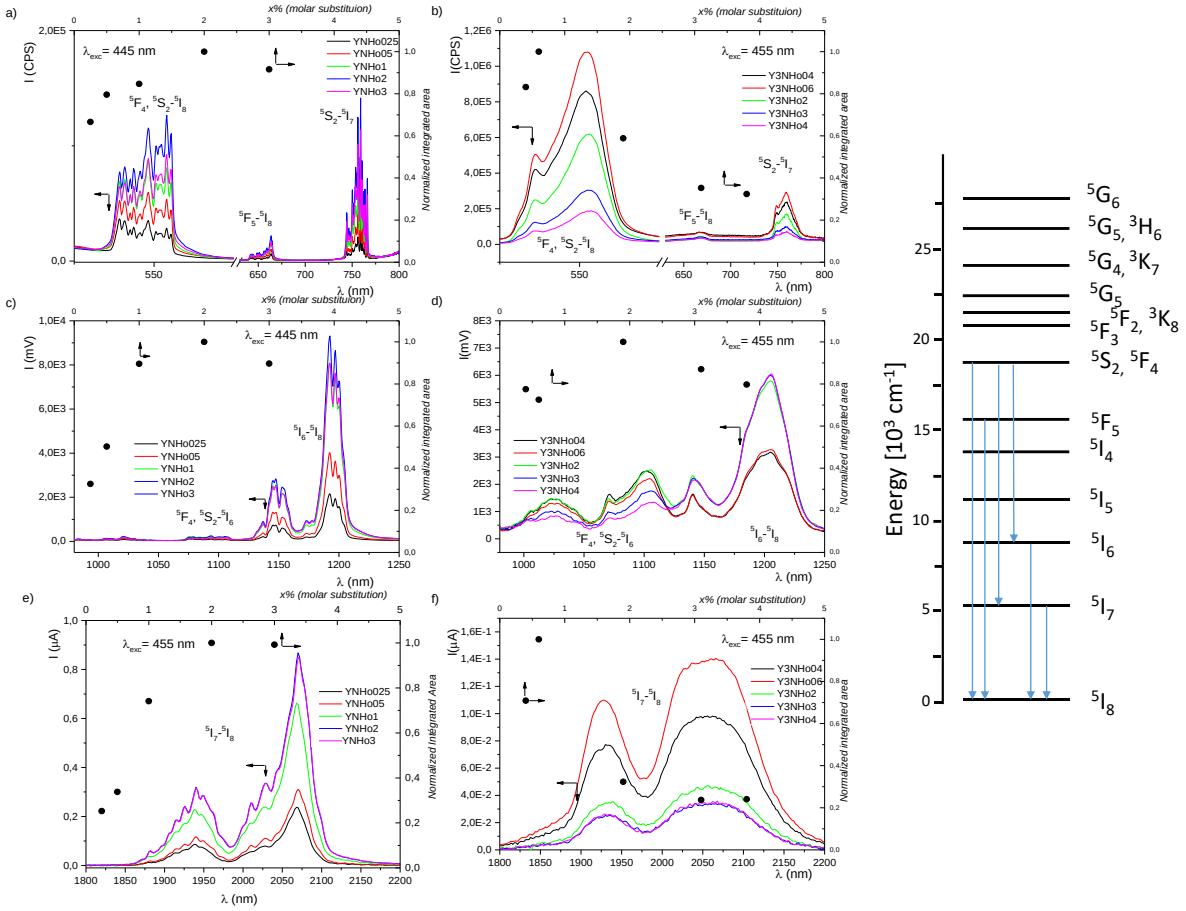

Figure 6- Emission of Ho^{3+}-doped compounds for samples with different Ho concentration (molar substitution rate) under excitation at 445 nm. Ho^{3+}-$YNbO_4$ powders (a,c,e), Ho^{3+}-Y_3NbO_7 powders (b,d,f). The relative error for the intensity is approximately 5% in the visible and approximately 10% in the infrared. The energy diagram of Ho^{3+} is shown on the right side of the figure.

For both materials, an equivalent spectral resolution was fixed to compare the spectral width of the transitions. Because of the local disorder induced by the oxygen vacancies in the vicinity of the doping element, the discrimination of the Stark components is not possible for the fluorite Y_3NbO_7. The maxima of intensity in the near- and mid-infrared equivalent for both materials

(the 2% Ho^{3+}-doped $YNbO_4$ compounds and the 0.6% Ho^{3+}-Y_3NbO_7) correspond to a close concentration of approximately 2.7 x10^{20} ions/cm^3 and 1.24x10^{20} ions/cm^3, respectively (Figure 6, black circles, top X-axis, right Y-axis). In the visible range, the green and red luminescence peaks at 550, 650, and 750 nm arise from the radiative de-excitation of the ($^5F_4$, $^5S_2$), $^5F_5$ and $^5S_2$ levels down to the $^5I_8$,$^5I_8$, and $^5I_7$ levels, respectively. The maximum near-infrared emission at 1.2 µm is assigned to the $^5I_6$-$^5I_8$ transitions and the 2 µm emission is assigned to the $^5I_7$-$^5I_8$ transitions. However, if the spectral distribution is constant for $YNbO_4$, a clear inversion of the $^5F_4$,$^5S_2$→$^5I_6$ and $^5I_6$→$^5I_8$ lines was detected at approximately 1 µm for the fluorite compounds, in agreement with the existence of a potential cross-relaxation process (CR1) between these levels [33]. The 2 µm emission of the fluorite Y_3NbO_7 is similar to that observed in a glassy environment as in Ho^{3+} doped germanate glasses whereas the Fergusonite $YNbO_4$ spectral distribution can be compared to the Ho^{3+} doped YAG crystalline phase [34,35].The impact of the local environment can be quantified by calculating the effective bandwidth, $\Delta\lambda_{eff}$. The 2 µm $\Delta\lambda_{eff}$ values were calculated using the following equation [36]:

$$\Delta\lambda_{eff} = \int \frac{I(\lambda)d\lambda}{I_{max}}.$$

The obtained $\Delta\lambda_{eff}$ values increase from approximately 145 nm to 200 nm for Ho^{3+}-doped $YNbO_4$ and Ho^{3+}-doped Y_3NbO_7, respectively, highlighting the rare earth environment distribution in these latest compounds.

The lifetime measurements were collected in the visible range for excitation at 445 nm and emission at 550 nm. The experimental data are presented in Figure 7, and the corresponding decay times are listed in Table 2.

A single-exponential law was used to adjust the decay curves of the Ho^{3+}-doped $YNbO_4$ compounds (Figure 7a). A decay time of 7.15 µs was obtained for the lowest concentration and a slight decrease in the decay time to 5.97 µs was observed for the highest concentrations. For fluorite compounds, a bi-exponential law is necessary to fit the experimental data. The two decay times were approximately 3 µs and 10 µs. These two contributions should reflect both the distribution of Ho^{3+} environments linked to the local disorder, and the existence of energy transfers between the elements leading to the cross-relaxation process mentioned above. Considering the similar results obtained for all Ho^{3+} concentrations in this study, the discrepancy in the values obtained for Y3NHo06 (longer decay times) is most likely due to the lower quality of the acquisition. The obtained values are of the same order of magnitude as those reported for Ho^{3+}-doped YAP and YAG oxide [37].

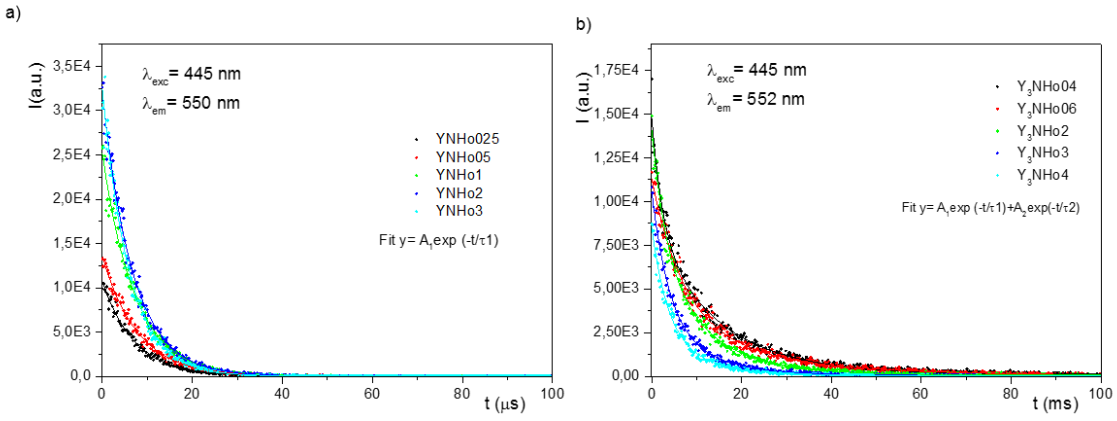

Figure 7- Decay curves of Ho^{3+}-doped compounds: Ho^{3+}-$YNbO_4$ (a); Ho^{3+}-Y_3NbO_7 (b). Dots represent the experimental points and solid lines show the mathematical fits.

Table 2- Decay times of the Ho^{3+}-doped niobate compounds

Ho^{3+}-doped $YNbO_4$		Ho^{3+}-doped Y_3NbO_7		
Samples	τ (µs)	Samples	τ1 (µs)	τ2 (µs)
YNHo025	7.15	Y3NHo04	2.43	14.68
YNHo05	7.80	Y3NHo06	6.67	21.15
YNHo1	7.20	Y3NHo2	3.16	11.30
YNHo2	6.73	Y3NHo3	3.73	10.72
YNHo3	5.97	Y3NHo4	3.37	9.29

Owing to the complexity of its energy diagram, different types of energy transfers can be activated through a high-power excitation source. Visible up-conversion from infrared excitation is often observed in Ho^{3+}-doped materials. This process includes emission, multiphonon relaxation, cross-relaxation between specific levels, ground state absorption (GSA), and excited state absorption (ESA). Several laser wavelengths are available to initiate such a transfer. A 640 nm laser pump (absorption at the $^5F_5$ level) was chosen by Redy et al. and Zhang et al. to excite Ho^{3+}-doped LaF_3 [38,39]. Such excitation results in blue and green up-conversion radiative de-excitation from the $^5F_3$ and $^5S_2$,$^5F_4$ levels at 416, 485, and 546 nm, respectively. The strongest emission is due to the green $^5S_2$,$^5F_4 \rightarrow {}^5I_8$ transition. These visible wavelengths were also detected under excitation at 800 nm [38]. Such excitation initiates a GSA process followed by multiphonon relaxation to successively populate the $^5I_5$ and $^5I_6$ levels. Then, the absorption of a second photon enables the population of the $^5F_3$ level to relax non-radiatively to the $^5S_2$, $^5F_4$ levels. An excitation at 752 nm in the $^5I_4$ level of Ho^{3+}-doped yttrium gallium garnet (YGG) gives rise to the green up-conversion emission (535–nm-557 nm). A weaker

emission was also reported between 623 and 671 nm [33] due to the $^5F_5 \rightarrow {}^5I_8$ transition. Rathaiah et al. proposed that after the $^5I_8$-$^5I_4$ GSA process, a non-radiative de-excitation through a multiphonon process populates the $^5I_6$ and $^5I_7$ levels. Successive ESA mechanisms from $^5I_6$ and $^5I_7$ populate the $^5G_6$, $^5F_1$, $^5S_2$, and $^5F_4$ levels, respectively. After multiphonon relaxation, green and red radiation are emitted. A near infrared source was selected by Wang *et al.* and Lin *et al.* to study the visible luminescence of Ho^{3+},Yb^{3+} co-doped BaY_2F_8 [40] and Ho^{3+}-doped (K,Na)NbO_3-$SrTiO_3$ [41], respectively. The co-doping improves the absorption of the 980 nm source by the Yb^{3+} ions. The absorption on the $^2F_{5/2}$ excited level of Yb^{3+} ions is followed by energy transfer to the $^5I_6$ level of Ho^{3+} ions. Under such excitation, a large number of Ho^{3+} cations transitioned from $^5I_6$ to $^5F_4$ and $^5S_2$ through ESA. The green emission remains at a maximum in comparison to the red emission. Lin et al. investigated the thermal behaviour of a Ho^{3+}-doped (K,Na)NbO_3-$SrTiO_3$ ceramic and the effect of the Ho^{3+} content. Both green and red emissions have been reported, but the concentration effect coupled with the temperature shows a thermal dependence of their relative intensity; an increased red contribution has been reported [41].

The Ho^{3+}-doped $YNbO_4$ and Y_3NbO_7 particles were excited at 975 nm, and the final results are shown in Figure 8. Under such excitation wavelengths, a phonon-assisted GSA process from the $^5I_8$ level may occur up to the $^5I_6$ level, as mentioned previously. The next step is the absorption of a second photon to the higher $^5F_4$ level through the absorption of one or more incident photons through an ESA process. Finally, electrons relax to the lower $^5S_2$ and $^5F_5$ levels by multiphoton relaxation.

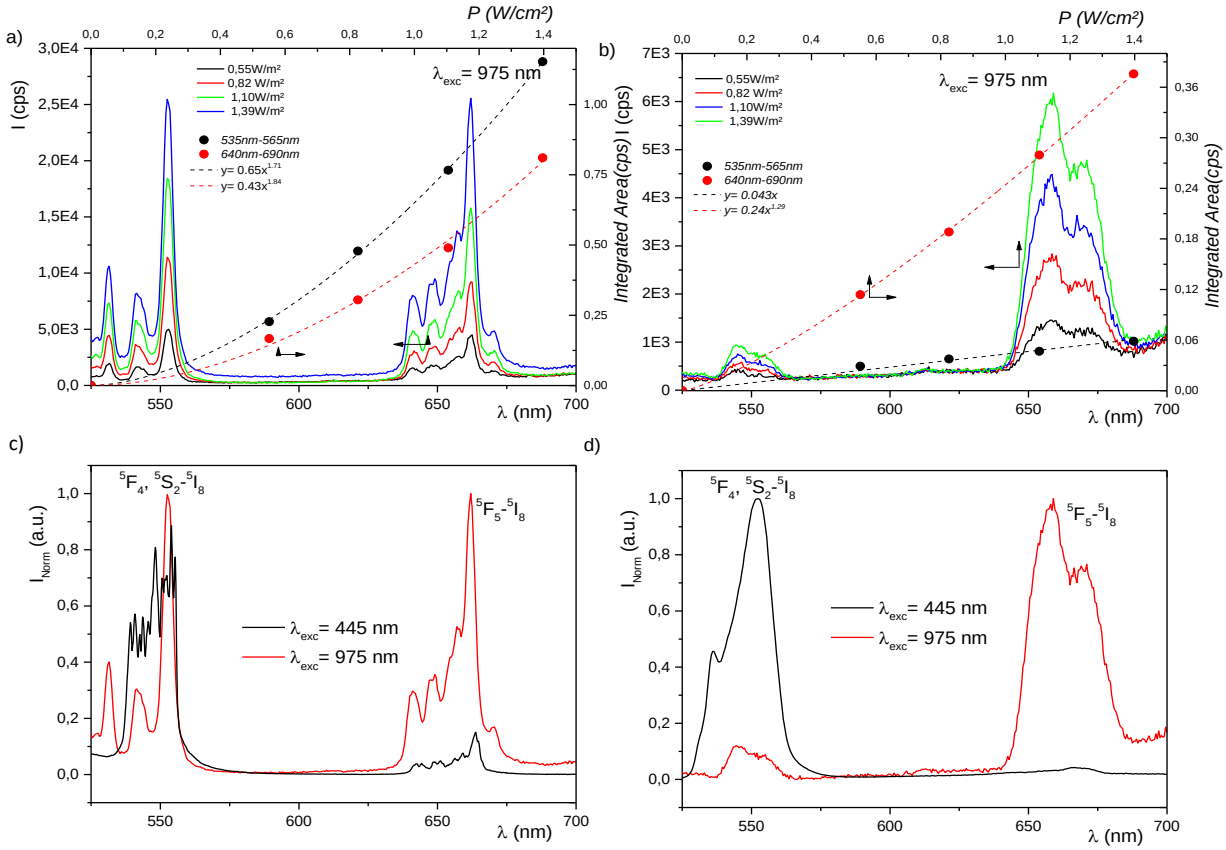

Figure 8- Up-conversion processes observed under excitation at 975 nm. Ho^{3+}-$YNbO_4$ powders (a,c); Ho^{3+}-Y_3NbO_7 powders (b,d),).

Then, green $^5S_2 \rightarrow {}^5I_8$ and red $^5F_5 \rightarrow {}^5I_8$ lines were clearly observed for both types of particles. The superposition of the emissions obtained at 445 nm and 975 nm is shown in Figures 8c and 8d. A significant change in the relative intensity was observed between the green and red emissions, and a higher red contribution was visible under infrared excitation. This results from a cross-relaxation process (CR2) from the neighbouring Ho^{3+} ions between the $^5F_4 \rightarrow {}^5F_5$ and $^5I_5 \rightarrow {}^5F_5$ transitions, leading to an increased population of the $^5F_5$ level from which the red $^5F_5 \rightarrow {}^5I_8$ transition is observed. This process appears to be much more significant for the Ho^{3+}-doped Y_3NbO_7 compounds, in agreement with the existence of the first CR1 process observed under 445 nm excitation. Niu *et al.* recently reported the up-conversion process observed under a 980 nm excitation source of the co-doped Ho^{3+}/Yb^{3+} $YNbO_4$ compound [42]. However, the proportion of green emission versus red emission appears much higher than that observed here. This should result in a higher population of the $^5F_4$ level due to energy transfer from Yb^{3+} ions; however, since no indication was given by the authors concerning the correction of the emission raw data (as mentioned before, the present data are corrected from the lamp spectral distribution

and the sensitivity of the detection), we cannot eliminate an underestimation of the red contribution owing to the lower sensitivity of the detector used as the origin of these results.

In addition, the integrated emission areas of the Ho^{3+}-doped niobate compounds were plotted as a function of the power of the incident source at 525–575 nm and 630–690 nm. The fit of the green and red up-conversion intensities of the Ho^{3+}-doped $YNbO_4$ exhibit a quadratic dependence with a slope of approximately 1.7, and 1.8, respectively. These values are slightly inferior to the values of 2 and 2.05 reported by Niu *et al.* [42] The deviation from the expected value of 2 is higher for the Ho^{3+}-doped Y_3NbO_7 with a slope of 1.29 for the red emission tends to confirm the contribution of the competitive processes as CR2 to the population of the $^5F_5$ level. The slope values of 1.87 and 1.57 were obtained by Wang *et al*. for the Ho^{3+}-doped BaY_2F_8 [40] for the blue and green emissions, respectively. The value of 1.5 is reported by Reddy *et al.* in the LaF_3 fluoride for the blue transition [38] and the value of 1.9 is reported for its green emission by Zhang *et al.*[39]. The global intensity of the green contribution is too weak to be significantly adjusted, as a linear law appears to be sufficient.

The different mechanisms of energy transfer identified in the studied niobate particles are shown in Figure 9.

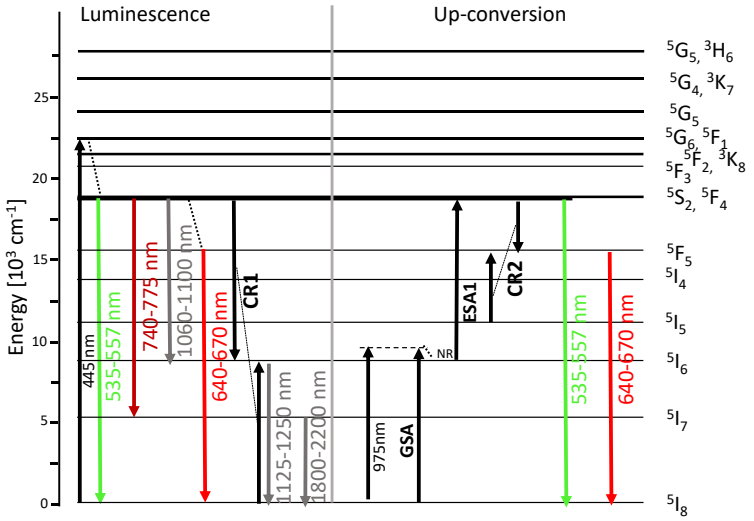

Figure 9- Energy transfers identified in the Ho^{3+}-doped niobate compounds

4- Conclusion

The spectral properties of pure Ho^{3+}-doped monoclinic $YNbO_4$ and cubic Y_3NbO_7 phases were reported and compared as a function of the dopant concentration. The yttrium/niobium ratio appears to play an important role in the stabilisation of a pure phase, the doping process, and the morphology and size of the particles. The $YNbO_4$ monoclinic phase is observed to be

stabilised at an earlier stage, leading to larger and higher crystallised grains. These experimental observations are supported by thermodynamic calculations that indicate a higher stability of the $YNbO_4$ phase. Its spectra show well-defined peaks, whereas the fluorite phase presents a wider spectral bandwidth that is assigned to the local disorder induced by the oxygen vacancies. In addition, for a similar Ho^{3+} content, the energy transfer observed at 445 nm or 975 nm is not equivalent for both materials, with a stronger interaction between the holmium cations found in the fluorite host lattice. The maximum intensity of 2 μm was not reached by the Ho^{3+}-doped $YNbO_4$ compound with the highest doping, meaning that a higher concentration is suitable for optimising this mid-infrared emission. In addition, the Ho^{3+}-doped Y_3NbO_7 fluorite exhibited a wider effective bandwidth. This enhancement should be beneficial for better absorption of the $^5I_7$ level under direct excitation with a 1.7-and 1.8 μm source. Consequently, a larger domain of laser tunability can be expected for compounds shaped as massive objects.

Acknowledgement

The authors thank the CNRS, the Nouvelle Region d'Aquitaine. This study was carried out with financial support of the Nouvelle Region d'Aquitaine (MISTRAL program n°2017-1R50311), in the frame of "the Investments for the future" Program IdEx Bordeaux – LAPHIA (ANR-10-IDEX-03-02) and the French Research National Agency (ANR program HEMERALD ANR-20-CE08-0016-01)

M. Nalin acknowledges the Brazilian funding agency FAPESP, grants (2013/07793-6 and 2019/01223-0).

References

[1] S. D. Jackson, Nat photonics, 149 (2012) 423-431 DOI: 10.1038/NPHOTON.2012.149
[2] Y. Tian, T. Wei, X. Jing, J. Zhang, S. Xu, Mat. Res. Bull. 76 (2016), 67-71, https://doi.org/10.1016/j.materresbull.2015.12.004
[3] D. Gelija, D.P.R. Borelli, , Mat. Res. Bull. 103 (2018) 268-278, https://doi.org/10.1016/j.materresbull.2018.02.052
[4] L. Bonnet, R. Boulesteix, A. Maître, C. Sallé, V. Couderc, A. Brenier, Optical Materials, 50(Part A) (2015) 2-10, https://doi.org/10.1016/j.optmat.2015.04.050
[5] W.X. Zhang, J. Zhou, W.B. Liu,J. Li, L. Wang, B.X. Jiang, Y.B. Pan, X.J. Cheng, J.Q. Xu, J Alloy Compd, 506(2) (2010) 745-748, https://doi.org/10.1016/j.jallcom.2010.07.059
[6] W. Li, H. Huang, B. Mei, J. Song, G. Yi, X. Guo, Mater Lett, 207 (2017) 37-40, https://doi.org/10.1016/j.matlet.2017.07.057
[7] X. Wu, J. Lin, P. Chen, C. Liu, M. Lin, C. Lin, L. Luo, X. Zheng, J Am Ceram Soc, 102(3) (2019) 1249-1258, DOI: 10.1111/jace.15967
[8] S. A. Payne, L. L. Chase, L.K. Smith, W.L. Kway, W. F. Krupke, IEEE J quantum elect, 28 (11) (1992) 2619-2630
[9] B. R. Reddy, S. Nash-Stevenson, P. Venkateswarlu, J Opt Soc Am B, 11(Issue 5) (1994) 923-927, https://doi.org/10.1364/JOSAB.11.000923
[10] G.H.Sun, Q.L.Zhang, H.J.Yang, J.Q.Luo, D.L.Sun, C.J.Gu, S.T.Yin, Mater Chem Phys 138(1) (2013) 162–166, DOI: 10.1016/j.matchemphys.2012.11.037

[11] Properties of lithium niobate, by K K Wong, editor London : INSPEC [Orig.-Prod.], (2002) Collection: Electronic Materials Information Service.; EMIS datareviews series
[12] J.O. Andersson, T. Helander, L. Höglund, P.F. Shi, B. Sundman, Thermo-Calc and DICTRA, Calphad 26 (2002) 273-312. https://doi.org/10.1016/S0364-5916(02)00037-8
[13] Thermo-Calc Software TCOX8 TCS Metal Oxide Solutions Database
[14] T. G. Babich, A. V. Zagorodnyuk, G. A. Teterin, L. V. Sadkovskaya, A. P. Zhirnova, Ukr. Khim. Zh. 55 (1989) 132–134. (translated Sov. Prog. Chem., 55(2) (1989) 21–24)
[15] J.-H. Lee, M. Yashima, M. Kakihana, M. Yoshimura, J. Am. Ceram. Soc., 81 (1998) 894–900, DOI: 10.1111/j.1151-2916.1998.tb02424.x
[16] S. W. Arulnesan, P. Kayser, J. A. Kimpton, B. J. Kennedy, J Solid State Chem, 277 (2019) 229-239, https://doi.org/10.1016/j.jssc.2019.06.014
[17] P. Sarin, R. W. Hughes, D. R. Lowry, Z. D. Apostolov, W. M. Kriven, J Am Ceram Soc, 97(10) (2014) 3307-3319 ,https://doi.org/10.1111/jace.13095
[18] T. Chraska, A. H. King, and C. C. Berndt, Mater. Sci. Eng., A, 286(1) (2000) 169–178
[19] R. C. Garvie, J. Phys. Chem., 69(4) (1965) 1238–1243
[20] R. C. Garvie, J. Phys. Chem., 82(2) (1978) 218-224
[21] R. C. Garvie, M. F. Goss, J. Mater. Sci., 21(4) (1986) 1253–1257
[22] A. Lauria, I. Villa, M . Fasoli, M. Niederberger, A. Vedda, ACS Nano, 7(8) (2013) 7041-7051
[23] M. Hirano, H. Dozono, J Am Ceram Soc, 96(11) (2013) 3389-3393, https://doi.org/10.1111/jace.12595
[24] H. Weitzel, H. Schroecke, Zeitschrift fuer Kristallographie Kristallstrukturverfeinerungen von Euxenit, 152 (1980) 69-p82, DOI:10.1524/zkri.1980.152.1-2.69
[25] P. Sarin, R.W. Hughes, D.R. Lowry, Z.D. Apostolov, W.M. Kriven, J. Am. Ceram. Soc., 97(10) (2014) 3307-3319, DOI: 10.1111/jace.13095
[26] H. J. Rossell, J. Solid State Chem., 27 (1979) 115–122, DOI: 10.1016/0022-4596(79)90150-6
[27] Y. Doi, Y. Harada, Y. Hinatsu, J. Solid State Chem., 182 (2009) 709–715, DOI: 10.1016/j.jssc.2008.12.012
[28] G. Blasse, J Solid State Chem.,7(2) (1973) 169-171
[29] L.A. Kinzhibalo, V.K. Trunov, A.A. Evdokimov, V.G. Krongauz, Kristallografiya+, 27 (1982) 43 translation S.E. Hall, Sov. Phys. Crystallogr. 27(1) (1982) 22-25
[30] S. W. Arulnesan, P. Kayser, J. A. Kimpton, B. J. Kennedy, J Solid State Chem. 277 (2019) 229-239
[31] A. Bertrand, J. Carreaud, G. Delaizir, M. Shimoda, J-R. Duclère, M. Colas, M. Belleil, J. Cornette, T. Hayakawa, C. Genevois, E. Veron, M. Allix, S. Chenu, F. Brisset, P. Thomas, *Cryst. Growth Des.* 15 (10) (2015) 5086–5096, https://doi.org/10.1021/acs.cgd.5b01048
[32] S.A. Kovyazina, L.A. Perelyaeva, I.A. Leonidov, Y.A. Bakhteeva, J Struct Chem+. 44 (2003) 975–979, https://doi.org/10.1023/B:JORY.0000034803.89136.ba
[33] M. Rathaiah, I.R. Martín, P. Babu, K. Linganna, C.K. Jayasankar, V. Lavín, V. Venkatramu, Opt Mater, 39(C) (2015) 16-20, DOI: 10.1016/j.optmat.2014.10.050
[34] X. Fan, P.0 Kuan,K. Li, L. Zhang, D. Li, L. Hu, Opt. Mater. Express, 5(6) (2015) 1356-1365, DOI:10.1364/OME.5.001356
[35] G. A. Kumar, M. Pokhrel, D.K. Sardar, P. Samuel, K-I. Ueda, T. Yanagitani, H. Yagi, Sci. Adv. Mater. 4(5/6) (2012), 617-622, https://doi.org/10.1166/sam.2012.1328
[36] C. Jiang, P. Deng, J. Zhang, G. Huang, F. Gan, J. Lumin., 82(4) (1999), 321-326, https://doi.org/10.1016/S0022-2313(99)00049-6
[37] M. Malinowski, M. Kaczkan, A Wnuk, M. Szufliñska, J Lumin., 106 (3–4) (2003) 269-279, https://doi.org/10.1016/j.jlumin.2003.10.008
[38] B. R. Reddy, S. Nash-Stevenson, P. Venkateswarlu, J Opt Soc Am B, 11(5) (1994) 923-927, https://doi.org/10.1364/JOSAB.11.000923
[39] X. Zhang, X. Liu, J-P. Jouart, G. Mary, J Lumin., 78(4) (1998) 289-293, https://doi.org/10.1016/S0022-2313(98)00005-2
[40] X. Wang, Y. Hou, J. Qu, J. Ding, H. Lin, L. Liu, Y. Zhou, F. Zeng, C. Li, Z. Su, J Lumin., 212 (2019) 154-159, DOI: 10.1016/j.jlumin.2019.03.055
[41] J. Lin, Q. Lu, J. Xu, X. Wu, C. Lin, T. Lin, C. Chen, L. Luo, J Am Ceram Soc,102 (2019) 4710-4720, https://doi.org/10.1111/jace.16336
[42] C. Niu, L. Li, X. Li, Y. Lv, X. Lang, Opt Mater, 75 (2018) 68-73, https://doi.org/10.1016/j.optmat.2017.07.001

Supporting information

Table SI1- ICP analyses – Cationic ratio of the Ho^{3+} doped Y_3NbO_7 compounds

		Y		Nb		Ho		nNb/(nHo+nNb+nY)
Sample	**m poudre**	**Cm (mg/L)**	***i***	**Cm (mg/L)**	***i***	**Cm (mg/L)**	***i***	**%Nb (mol)**
0%	0,0104	88	*4,3*	26,95	*3*	0	*2,59*	**22,7**
1%	0,0106	90,39	*4,3*	27,45	*3*	0,85	*2,59*	**22,4**
2%	0,0104	91,73	*4,3*	26,58	*3*	1,32	*2,59*	**21,6**
5%	0,0101	85,39	*4,3*	26,22	*3*	3,89	*2,59*	**22,3**
8%	0,0116	87,24	*4,3*	28,23	*3*	6,68	*2,59*	**22,9**
10%	0,0105	77,39	*4,3*	26,52	*3*	7,6	*2,59*	**23,7**

i: error

Figure SI1

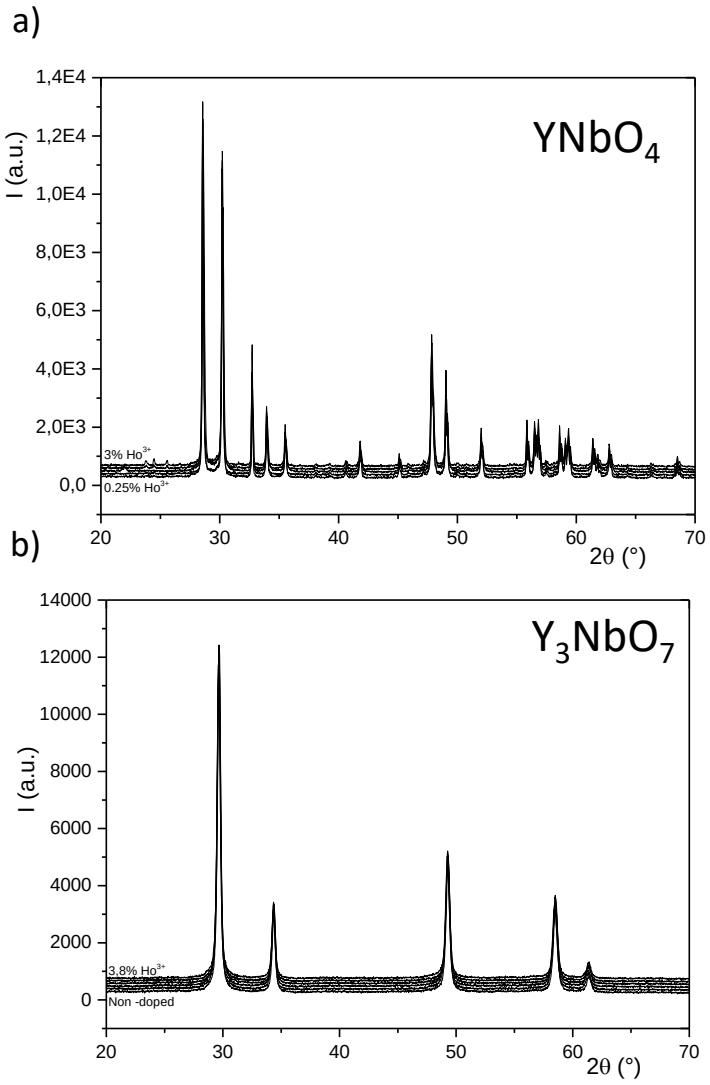

Figure SI1- Diffractograms of Ho^{3+} doped niobate compounds as function of the Ho^{3+} concentration. Ho^{3+} doped $YNbO_4$ were heat-treated at 1300 °C (a) whereas Ho^{3+} doped Y_3NbO_7 were heat-treated at 1100 °C.